metals

Article

Numerical Simulation of Multi-Physics Fields in Fused Magnesia Furnace

Tianchi Jiang and Weijun Zhang *

State Key Laboratory of Environmental Ecology, Northeastern University, Shenyang 110168, China
* Correspondence: zhangwj@smm.neu.edu.cn

Abstract: In this paper, a 3D transient multi-physical field model is developed to capture the complex processes inside a fused magnesia furnace. The multi-physics model integrates electromagnetism, thermodynamics, decomposition reactions, and flow. The three-phase submerged magnesia furnace includes an arc, magnesite ores, a melting pool, and a solidification ingot. For a more comprehensive analysis of the optimal design of industrial operations, the influence of the key index of electrode insertion depth on temperature and reaction is also discussed. The results show that the current density in the fused magnesia furnace is almost the same as the joule heat distribution, and there is an obvious area of low energy density affected by the skin effect, which leads to the waste of electric energy. The temperature at the center of the arc reaches 12,000 K, and the plasma areas formed at the end of the three electrodes are connected to each other to form a closed current path, which provides energy for the process of melting magnesia. The arc region is an ellipsoid with a length of ~30 mm and a diameter of ~49 mm. The decomposition reaction of magnesite mainly occurs in the arc area, and the radiation heat provided by the high-temperature arc is used as the heat source. There is almost no magnesite in the molten pool, and the molten pool only provides energy for the melting process of magnesia. When the electrode insertion depth is 0.4, 0.5, 0.6, and 0.7 m, the arc length is 0.049 m, 0.066 m, 0.068 m, and 0.059 m, respectively. According to the simulation results, there is an optimal electrode insertion depth.

Keywords: fused magnesia; multi-physical fields; numerical simulation; parameter analysis

Citation: Jiang, T.; Zhang, W. Numerical Simulation of Multi-Physics Fields in Fused Magnesia Furnace. *Metals* **2023**, *13*, 39. https://doi.org/10.3390/met13010039

Academic Editor: Mahesh Somani

Received: 30 October 2022
Revised: 8 December 2022
Accepted: 14 December 2022
Published: 23 December 2022

1. Introduction

Fused magnesia furnaces are widely used in the fused magnesia industry and have great energy-saving potential [1]. In the production of fused magnesia, magnesite is smelted by a fused magnesia furnace [2]. The interior of a fused magnesia furnace consists of a graphite electrode, a plasma arc area, ore raw material, a fused magnesia product, sand, and furnace gas, with carbon dioxide as the main component. The arc heat at the end of the electrode is the main heat source of magnesium oxide furnaces [3].

The arc is the most important research object in a fused magnesia furnace. Since physical phenomena in the furnace cannot be observed, the thermal effect, power consumption, energy efficiency, and other characteristics of the arc are studied. Bowman et al. used shock wave technology to measure the radial temperature distribution of a natural alternating current arc column, and the results showed that, at any point in the arc column, the temperature had a certain average value, and a circulating heat wave phenomenon could be observed [4]. Wu et al. established a two-dimensional axis-symmetric mathematical model for fixed keyhole plasma arc welding and numerically calculated the coupling between the arc and the molten pool at a high-temperature flow. The calculation results obtained via this numerical method were highly similar to the experimental results [5]. In order to control the content of Cr_2O_3 in electric arc furnaces, Aula et al. analyzed the content of Cr_2O_3 in slag during EAF operation by measuring the emission spectrum of the arc. The results showed that, by using Ca l, Fe l, and Mn l as the references of Cr l, the best accuracy could be obtained, and the error was 0.62% [6]. Cayo et al. designed an arc welding monitoring system for tungsten inert gas welding processes and conducted experiments in different locations, and the results showed that arc emissions can be used to monitor and detect interference in the welding process [7]. Almurr et al. studied the influence of an external magnetic field on the arc generated by the disconnection of low-voltage switch contacts using the numerical model developed by COMSOL and compared the numerical calculation results with the numerical results of specially designed test equipment to better understand the physical phenomena involved [8]. Urusov et al. established a three-dimensional mathematical model framework of local thermodynamic equilibrium, calculated the characteristics of arc combustion with a uniform external axial magnetic field, and proposed a method of direct current arc simulation [9]. Chi et al. calculated the equilibrium composition and thermodynamic parameters of gas and its mixture plasma under a local thermodynamic non-equilibrium state, proposed an improved Levenberg–Marquardt algorithm, and summarized a series of thermodynamic parameters for magnesium–air plasma, which provided the basis for the physical parameters in this paper [10]. Deng et al. developed an magnetohydrodynamic model to simulate the multi-physical field of DC arc plasma under turbulent and laminar flow conditions, and the simulation results were consistent with the corresponding experimental results. The results showed that the operation under laminar flow conditions could improve the total thermal efficiency of the torch [11]. Wen et al. developed a 3D time-dependent numerical model based on the assumption of local thermodynamic equilibrium to study the arc dynamics and its distribution of temperature and flow field inside and outside the torch, and the relevant calculation results were verified experimentally [12].

Some studies on the melting state in EAFs have also been carried out. Wang et al. established a steady-state three-position magnetohydrodynamic model and calculated the flow state in the arc area of a DC molten magnesium oxide furnace, and the results showed that the molten pool was shaped like a crater sag [13]. In addition, Wang et al. also studied the temperature field in fused magnesia furnaces with different power densities, and the results showed that a higher power electric energy input would cause more drastic liquid level fluctuations and that a large-capacity electric arc furnace has advantages in energy saving and production efficiency improvement [14]. Yu et al. studied the complex multiphase reaction in a three-phase submerged arc furnace; developed a numerical calculation model considering the electromagnetic field, flow, and chemical reaction; and studied the influence of electrode insertion depth. The results showed that the arc temperature of the three-phase arc furnace used for smelting chromite pellets was 5897.17 K. The optimal insertion depth was determined for the simulation results [15]. Xi et al. established a mathematical model to analyze the smelting process of scrap steel, fully considered the influence of the number of steel electrodes and the porosity of scrap steel on the smelting speed, and obtained the conclusion that multiple electrodes can significantly improve the smelting effect and that the smelting speed of multiple electrodes is similar to that of a single electrode when the porosity is greater than 0.84 [16]. Logar et al. studied AC arc furnace electric system design and the control of process optimization. Their theoretical research on electrical, chemical, and thermal properties reflect the characteristics of the AC arc furnace parameters and has established mathematical models of phase fitting with the experimental results. Their paper proposed a feedback model from a combination of theory and practice, which provided a basis for subsequent control design [17]. Yang et al. studied the velocity distribution and temperature distribution in EAFs with bottom-blowing technology. Their paper introduced the development of a 3D multiphase flow numerical model, and the results showed that the bottom-blowing scheme with a linear change in the gas rate had the best stirring effect in the molten pool [18]. Zhang et al. developed a two-dimensional model coupled with electromagnetic stirring and the thermodynamic theory to calculate the aluminum alloy smelting process, and the results showed that the horizontal rotating electromagnetic field and denser velocity field made the temperature difference in the stirred melt smaller [19]. Wang et al. established a unified mathematical model and calculated key parameters, such as the molten pool, weld, velocity, and current density of two-electrode TIG arc heat sources, and the simulation results were consistent with the experimental results [20].

According to the above literature, in metallurgy, welding, and other fields, the multi-physical field parameters involved in furnaces and the mathematical models of the distribution of the multi-physical field have been extensively studied. Numerical simulation technology based on the multi-physical field is an advanced method used to predict the state in a furnace. However, in the field of fused magnesia, to the best of our knowledge, no successful attempt has been made to incorporate all the necessary factors into a coupled numerical simulation model to predict the current complex industrial processes of fused magnesia. In the present work, a transient multi-physical field model incorporating decomposition reactions is developed. In the stable operation of a fused magnesia furnace, the multiple physical fields of the arc and charge at different temperatures are discussed. The multi-physics field model can provide more information on a fused magnesia furnace. In this model, the physical properties of the plasma in the AC arc region are fully considered, which is the most neglected part in many studies on electric arc furnaces. In addition, a parametric study is carried out to analyze the sensitivity between the electrode insertion depth of several parameters of a furnace. The strategies that can improve the smelting state of a fused magnesia furnace are also discussed. The innovations of this paper are as follows:

1. Based on the actual production of fused magnesium oxide, a three-dimensional transient electromagnetic heat flow multi-field coupling model is established to feedback the production state in a furnace.
2. The assumption that a furnace is all magnesium oxide in many previous works is removed, and the influence of chemical reactions on temperature distribution is fully considered.
3. The frequently used interpolation method is abandoned, and a more accurate two-way coupling method is selected to define the source term of the electromagnetic field equation in the form of user defined functions.

2. Mathematical Model

2.1. Multi-Physics Field Model

In a fused magnesia furnace, multiple physical fields are closely coupled. In most industrial fused magnesia systems, the conditions in the furnace of the smelting process are unknown. The existing instruments can measure the instantaneous voltage and current of the secondary side of the transformer, the temperature of the outer wall of the mold, and the temperature of the upper surface of the stacked material. Although magnesite is not conductive, the arc initiator located at the bottom of the charge provides a reasonable arc starting distance for the three-phase electrode. The air is excited to the plasma state first. The energy provided by the high-temperature plasma arc is used to melt the magnesite and support the decomposition reaction, and it provides a closed conductive loop for the three-phase electricity. In the process of smelting, a small amount of gaseous magnesia will be transformed into plasma magnesia, and the arc composition in a fused magnesia furnace is a mixture of air plasma and magnesia plasma. In the current arc calculation model, the input power of the electrode is generally considered to be equal to the heating power of the plasma, but, in fact, the heat used to melt and decompose the ore is less than the input power of the electrode, and the difference between them is equal to the energy required for the formation and heating of the plasma. Due to the process of fused magnesia being an isobaric process, in order to accurately solve the energy value of air and magnesia excitation, enthalpy change and different temperatures of enthalpy values are calculated using a simplified Marquardt algorithm and coupled to the corresponding electromagnetic field in the model [10].

In the current research, two main coupling modes of the electromagnetic field, energy, and momentum equations exist. First, the simplified Maxwell equations are coupled to

FLUENT using the magnetic vector potential method in order to realize the coupling of the electromagnetic field, temperature field, and velocity field. Second, the electromagnetic field and temperature field are calculated using MAXWELL or ANSYS commercial software, and then the temperature of each node is interpolated to the grid node in FLUENT so as to realize the unidirectional coupling of the electromagnetic field, temperature field, and flow field. Since the second calculation method treats the unsteady heat source of the alternating current as the steady heat source, which is unreasonable, the first calculation method is adopted in this paper.

In addition, the multi-physical field coupling model is also introduced in this part. The electromagnetic field equation is substituted into the energy equation, momentum equation, and mass balance equation via the form of source terms. The furnace mainly contains magnesite, molten, and liquid magnesium oxide. The average diameter of the particles is 19.7 mm, the porosity is 0.4, and the resistance of the porous medium is added into the equation as a source term.

According to Gauss's law of magnetism,

$$\nabla \times \vec{B} = 0 \tag{1}$$

where B represents the magnetic induction intensity (T).

The magnetic vector potential can be expressed as

$$\vec{B} = \nabla \times \vec{A} \tag{2}$$

$$\vec{A} = \mu_0 \vec{J} \tag{3}$$

where $\vec{A}$ is the magnetic vector potential (V s/m), and μ_0 is the vacuum permeability $4\pi \times 10^{-7}$ (T m/A).

According to Ohm's law,

$$\vec{J} = \sigma \vec{E} \tag{4}$$

where $\vec{J}$ represents the current density (A/m^3), σ represents the conductivity (S/m), and $\vec{E}$ represents the electric field strength (V/m).

The electric field strength of the spineless part can be expressed as

$$\vec{E} = -\nabla \varphi \tag{5}$$

where φ denotes the electric potential (V).

According to Faraday's law of electromagnetic induction, the strength of the electric field with rotation is

$$\nabla \times \vec{E} = -\frac{\partial \vec{B}}{\partial t} = \nabla \left(-\frac{\partial \vec{A}}{\partial t} \right) \tag{6}$$

Therefore, the electric field strength can be expressed as

$$\vec{E} = -\nabla \varphi - \frac{\partial A}{\partial t} \tag{7}$$

where t is time (s).

In the transient state, the continuity equation is as follows:

$$\frac{\partial \rho}{\partial t} + \nabla \left(\rho \vec{u} \right) = 0 \tag{8}$$

where ρ is the density (kg/m^3), and $\vec{u}$ is the velocity vector (m/s).

The momentum conservation equation has the following form [15]:

$$\frac{\partial\left(\rho\vec{u}\right)}{\partial t}+\nabla\bullet\left(\rho\vec{u}\vec{u}\right)=-\nabla p+\mu\nabla\bullet\left(\nabla\vec{u}\right)+\rho g+\vec{F_E}+S_d \tag{9}$$

where μ is the dynamic viscosity (Pa s), $\vec{F_E}$ is the electromagnetic force (N/m^3), g is the gravitational acceleration (m/s^2), and S_d is the resistance source term produced by the porous medium.

The $\vec{F_E}$ expression is as follows:

$$\vec{F_E}=\vec{J}\times\vec{B} \tag{10}$$

The S_d expression is as follows:

$$S_d=-\left(\frac{\mu}{\alpha}\bullet\vec{u}+\frac{1}{2}C_2\rho\vec{u}\vec{u}\right) \tag{11}$$

where d represents the components in x, y, and z directions, and a represents the permeability coefficient. C_2 represents the resistance coefficient. $\vec{u}$ represents the velocity vector perpendicular to the porous media surface.

The energy conservation equation has the following form [21]:

$$\frac{\partial}{\partial t}(\rho H)+\nabla\bullet(\rho u H)=\nabla\bullet\left(k_{eff}\nabla T-\sum_j h_j\vec{\sigma_j}+\tau_{eff}\bullet\vec{u}\right)+Q_{elec}+Q_{rad}+Q_{reac} \tag{12}$$

where u is the velocity flowing through the unit (m/s), k_{eff} is the thermal conductivity [w/(m*K)], h_j is the diffusion coefficient of different components, τ_{eff} is the viscosity coefficient, Q_{rad} is the radiation heat, Q_{reac} is the reaction heat, H is the enthalpy (J/kg), and Q_{elec} is the heat provided by the arc to the system (W/m^3). The calculation method is as follows:

$$H=C_pT+\frac{p}{\rho} \tag{13}$$

where Cp is the specific heat [J/(kg*K)], p is the pressure (pa), and T is the temperature (K).

$$Q_{elec}=\frac{\vec{J}\bullet\vec{J}}{R_{plasma}}-Q_{rad} \tag{14}$$

R_{plasma} is the resistance of the plasma.

Q_{rad} is the radiant heat loss, and it is calculated as follows:

$$Q_{rad}=aG-4an^2\delta T^4 \tag{15}$$

where q_k is the heat absorption of the different reactions, Δc_k is the change in mass fraction, M_k is the number of moles of reactants, and Δt is the time step.

The heat of the reaction is calculated as follows:

$$Q_{reac}=\sum_k\frac{q_k\Delta c_k\rho}{M_k\Delta t} \tag{16}$$

where q_k is the heat absorption of different reactions, Δc_k is the change in mass fraction, M_k is the number of moles of reactants, and Δt is the time step.

The component equation is as follows:

$$\frac{\partial}{\partial t}(\rho w_i)+\nabla\cdot(\rho\vec{v}w_i)=-\nabla\vec{J_i}+R_i \tag{17}$$

where R_i is the net formation rate of component i, and w_i is the mass fraction of the component.

J_i is calculated as follows:

$$\overrightarrow{J_i} = -\left(\rho D_{i,m} + \frac{\mu_t}{0.7}\right)\nabla w_i - D_{T,i}\frac{\nabla T}{T} \tag{18}$$

$D_{i,m}$ is the mass diffusion coefficient, and $D_{T,i}$ is the thermal diffusion coefficient.

The source terms of the purification components produced by chemical reactions are calculated as follows:

$$R_i = M_{w,i}\sum_{r=1}^{n} R_{i,r} \tag{19}$$

Since the chemical reaction involved in this paper is a decomposition reaction, the reaction process is irreversible, so

$$R_{i,r} = \left(v'_{i,p} - v'_{i,r}\right)\left[k\prod_{i=1}^{N}\left(c_{i,r}\right)^{\eta'_{i,r}}\right] \tag{20}$$

where $v_{i,p}$ represents the product stoichiometry, $v_{i,r}$ represents the reactant stoichiometry, $c_{i,r}$ represents the molar distribution, and $\eta'_{i,r}$ represents the rate exponent.

The k of the reaction progress is calculated as follows [22]:

$$k = Ae^{(-E_a/RT)} \tag{21}$$

where A is the leading factor, E_a is the activation energy of the chemical reaction, and R is the ideal gas state parameter.

2.2. Simulation Assumption

a. Under actual conditions, the operation mode of a fused magnesium oxide furnace is intermittent feeding. However, in the model, the calculation domain is initially filled with ore, the furnace gas diffuses upward, and the product diffuses downward; moreover, the cooling process after smelting is not included in the calculation scope.
b. Chemical reactions of primary concern are considered, and very few additional reactions are ignored.
c. Arc composition is considered to be a mixture of air plasma and magnesium oxide plasma, and its physical parameters obtained from [10].
d. Since the mold wall thickness in the fused magnesium oxide furnace is only 3 mm, its physical model is ignored, and the fixed heat flux is replaced.
e. Gas products are considered to be incompressible ideal gases.
f. Plasma is considered to be a liquid with unique physical properties. Other properties are not taken into account.

3. Simulation Strategy

3.1. Geometry

The structure of a fused magnesia furnace is shown in Figure 1. The purpose of this paper is to study the decomposition process of magnesite under the action of electric arcs and the distribution of multiple physical fields in the furnace. Therefore, the calculation area is the area inside the fused magnesium oxide furnace. Specific structural parameters are listed in Table 1. It is worth mentioning that, although the height of the conventional furnace body is 5 m, a crystallizer with a height of only about 1.2 m is used in the initial stage of production, which is constantly superimposed to 5 m in the smelting process, so only the height of 1.2 m is considered in the calculation domain.

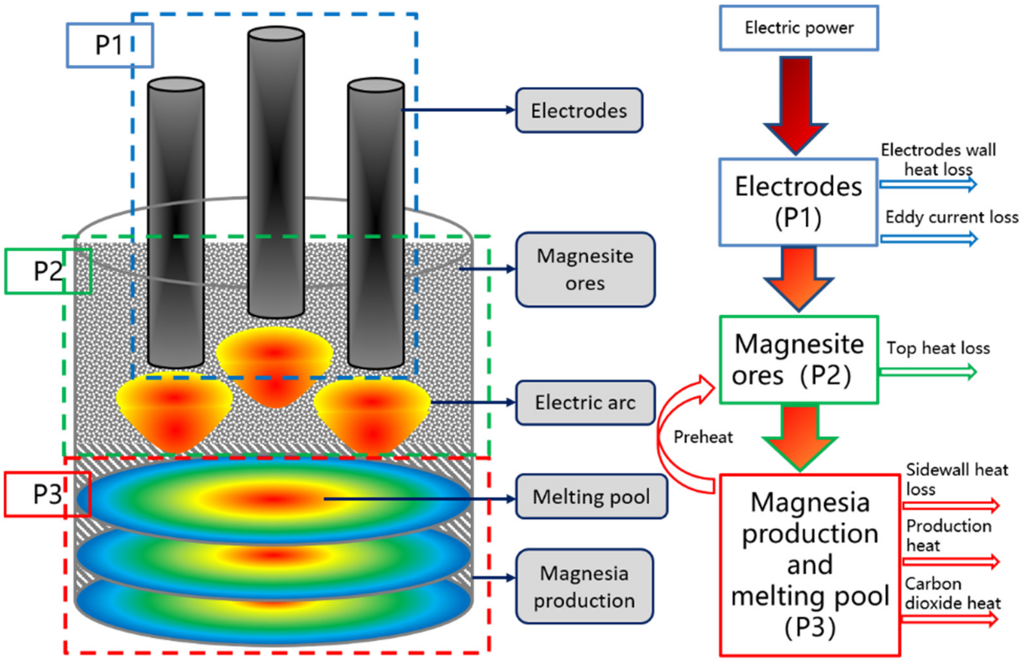

Figure 1. Schematic diagram of the fused magnesia furnace.

Table 1. Furnace parameters.

Parameters	Value
Furnace height	1.2 m
Furnace diameter	1.9 m
Electrode diameter	0.2 m
Electrode length	1 m
Electrode insertion depth	0.5 m
Wall thickness	0.003 m

The main structure of the molten magnesium oxide furnace includes an electrode part (P1), an ore and arc part (P2), a molten pool, and a solidified billet part (P3). P1 mainly includes the electrode and electrode holder, P2 mainly includes the magnesite and excited arc, and P3 mainly consists of the molten magnesia and solidified magnesia products.

3.2. Physical Properties

For magnesia smelting, the charge contains fused magnesia, heavy burned magnesia, and light burned magnesia. The main reason for this is that the temperature difference in a furnace is large. When the temperature exceeds 3000 K, magnesia is remelted to form fused magnesia, which is mostly distributed in the center of the product. When the temperature is 1600 K to 3000 K, magnesia is calcined to form heavy burned magnesia, and the products are mostly distributed on the surface of solidified billet. When the temperature is 900 K to 1600 K, magnesite is decomposed into light burned magnesia, and the product is distributed on the top of the solidification billet.

Magnesite is broken to about 50 mm. The porosity of the particles is about 0.3. Figure 2 shows more details of the magnesite. The physical characteristics are related to temperature, the physical parameters of conventional substances obtained from [21], and the physical parameters of plasma obtained from [10].

Figure 2. Furnace charged for smelting.

Tables 2–4 show the chemical reactions, basic thermal physical parameters, and arc physical parameters of the special complex components that need to be considered in the process of fused magnesia, respectively. These data are directly used to calculate the final field distribution.

Table 2. Reduction reaction.

	Reaction	Temperature (K)	A (min^{-1})	Ea (kj/mol)	Absorb Heat (kj/mol)
1	$MgCO_3$ = MgO (light burned) + CO_2	>973	3.22×10^6	79.10	100.59
2	MgO (light burned) = MgO (die burned)	973–2873	-	-	-
3	MgO (die burned) = MgO (fused)	>2873	-	-	-

Table 3. Physical parameters of magnesium oxide.

Physical Parameters	Value
Temperature (K)	T
Density (kg/m^3)	3580
Heat capacity [J/(kg·K)]	$Cp = 48.99 + 3.14 \times 10^{-3}T - 11.72 \times 10^5 T^{-2}$
Thermal conductivity [W/(m·K)]	$\lambda = 1.1 \times 10^{-11}T^4 - 0.2267T + 100$
Electrical conductivity (S/m)	19,894.5

Table 4. Arc physical parameters.

Temperature (K)	Density (Kg/m^3)	Heat Conductivity (W/m·K)	Electric Conductivity (S/m)	Viscosity (Kg/m·s)	Radiation Coefficient (W/sr·m^3)	Capacity (J/Kg·K)
3000	105.999	0.6	19,894.6	0.00792	7.214	131.3
5000	89.23	1.01	115,856.3	0.0011	47.265	288.4
7000	28.26	1.44	216,795.8	0.0012	427.977	3601.8
9000	17.39	1.51	477,875.8	0.00065	1158.582	16,136.5
11,000	11.89	1.74	525,808.8	0.00049	4990.26	22,768.5
13,000	9.00	2.15	624,092.1	0.0004	9303.39	56,605.7

3.3. Boundary Conditions

The boundary conditions of the furnace are listed in Table 5. Since the voltage is kept constant in the smelting process, the conductivity of the ore, magnesia, and arc in the furnace changes with the temperature, so the temperature in the furnace and the change in current density and material properties affect each other. The maximum potential at the electrode is determined by the value of the secondary side of the transformer, the frequency is 50 Hz, and the phase difference between the electrodes is 120°.

Table 5. Boundary conditions.

Boundary	Voltage (V)	Magnetic Potential Vector (Vsm^{-1})	Temperature (K)
Electrode A	$\varphi_1 = V_1 \times \sin(2\pi \times f \times t)$	$\frac{\partial \vec{A}}{\partial \vec{n}} = 0$	5000
Electrode B	$\varphi_2 = V_2 \times \sin(2\pi \times f \times t + \frac{2\pi}{3})$	$\frac{\partial \vec{A}}{\partial \vec{n}} = 0$	5000
Electrode C	$\varphi_1 = V_3 \times \sin(2\pi \times f \times t + \frac{4\pi}{3})$	$\frac{\partial \vec{A}}{\partial \vec{n}} = 0$	5000
Electrode sidewall	$\frac{\partial \varphi}{\partial n} = 0$	$\frac{\partial \vec{A}}{\partial \vec{n}} = 0$	2300
Furnace top surface	$\frac{\partial \varphi}{\partial n} = 0$	$\frac{\partial \vec{A}}{\partial \vec{n}} = 0$	$-\lambda \times \frac{\partial T}{\partial n} = 2 \times (T - T_0)$
Furnace sidewall	$\frac{\partial \varphi}{\partial n} = 0$	$\vec{A} = 0$	$-\lambda \times \frac{\partial T}{\partial n} = 10 \times (T - T_1)$
Furnace bottom	$\varphi = 0$	$\frac{\partial \vec{A}}{\partial n} = 0$	$-\lambda \times \frac{\partial T}{\partial n} = 2 \times (T - T_2)$

The initial state of the simulation is standard air pressure, 298.15 K, and all the ore is accumulated in the furnace.

3.4. Numerical Procedure

The model combines heat transfer, the decomposition reaction, turbulence flow, and electromagnetic field distribution. FLUENT commercial software (14.5, ANSYS, Shenyang, China) is used for numerical calculations. Since the physical parameters of the arc are quite different from those of the fluid in the conventional state, the PISO algorithm with more stable calculation is selected for calculation. After initialization, the equation is discretized using the first-order upwind scheme, and then the second-order upwind scheme is used for calculation after the calculation is stable. Because the arc Reynolds number is much larger than 2300, the standard $k - \varepsilon$ model is used to describe the arc. The radiation is calculated using the P1 radiation model. The time step is 0.01 s.

4. Results and Discussion

A three-dimensional transient multi-physical field model is applied to test and describe the smelting state of magnesite in the decomposition process, and the calculation time is 1500 s. The current density distribution, joule heat distribution, arc distribution, reaction position, and other information are discussed. In addition, the influence of the electrode insertion depth on the relevant results is also discussed.

4.1. Model Simplification and Mesh Generation

According to the computational requirements of this study, the model is simplified:

a. The electrode part is simplified and replaced by the potential inlet at the end of the electrodes because the graphite electrodes have a low resistivity, and its voltage drop of only 4 V does not affect the results too much.

b. Since the iron plate is thin, the temperatures of the inner and outer walls of the iron plate are similar, so it is of little significance to study the radial temperature distribution of the cylindrical iron plate. In order to simplify the calculation, the 3 mm-thick iron plate is simplified as a wall surface in the physical model, and the wall thickness is set as 3 mm in fluent during the numerical calculation.

After simplification, the whole model is discretized using structural mesh, and the electrode end is refined to improve the accuracy of the calculation. The mesh results are shown in Figure 3.

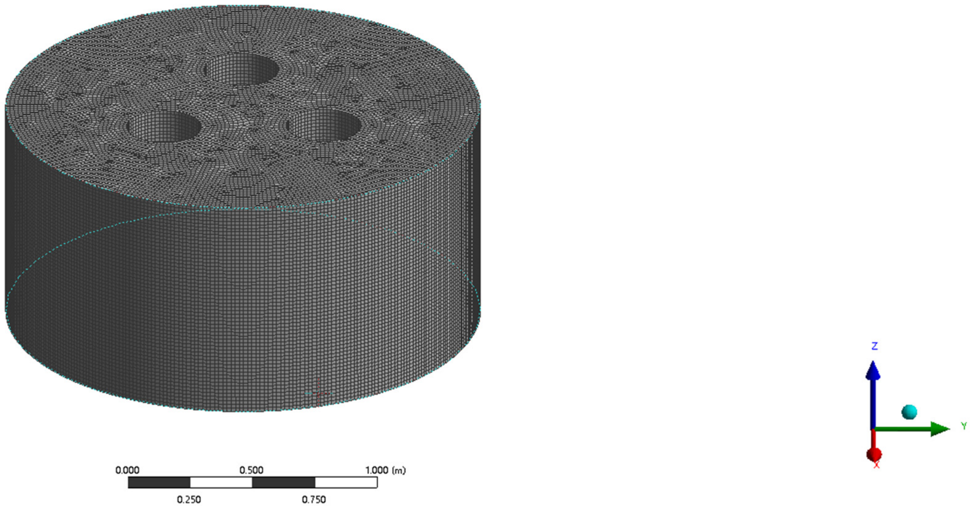

Figure 3. Mesh distribution.

A structured mesh is used to discretize the computational area, and local mesh encryption is performed at the end of the electrode. The amount of mesh has a direct impact on the calculation accuracy and time, which requires a mesh independence calculation to determine the optimal number of meshes. The numbers of the grids for independence verification are N1 = 4.3×10^5, N2 = 6.7×10^5, N3 = 9.6×10^5, and N4 = 11.1×10^5.

The section shown in Figure 4 is selected, and the temperature along the section length direction at z = 0.69 m is compared. When the number of grids increases to 96 w, the data distribution basically remains the same, so 96 w grids are selected for calculation.

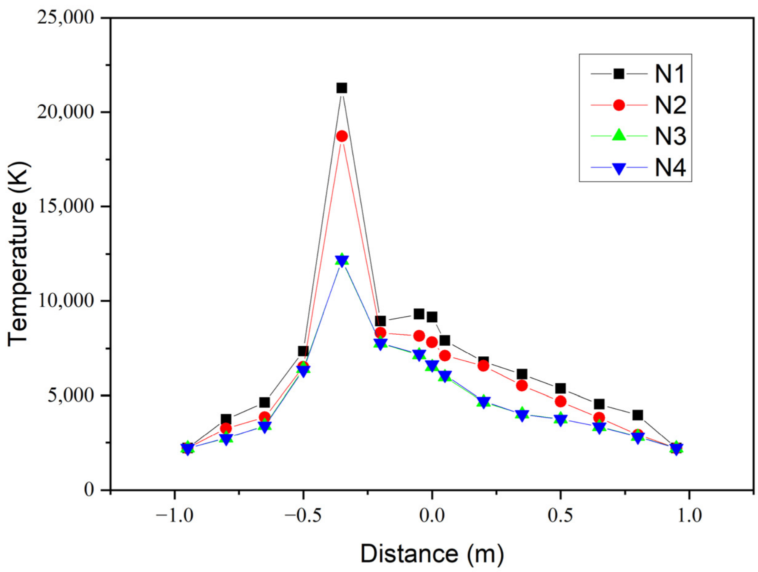

Figure 4. Grid independence verification results.

4.2. Model Validation

In this paper, the same two-dimensional physical model was established based on the BOWMAN experiment, and the simulation calculation was carried out [23]. The numerical calculation results based on the mathematical model in this paper were compared with the arc speed of 2160 A measured in BOWMAN's high-current arc experiment in Figure 5, with the purpose of verifying the accuracy of the model. As can be seen in the figure, the simulated arc velocity results are consistent with the experimental results, which reflects the accuracy of the model to a certain extent.

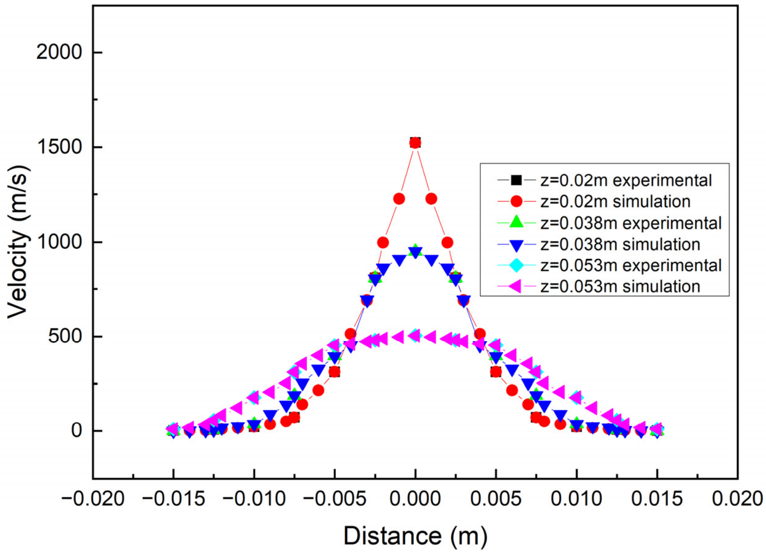

Figure 5. Accuracy verification.

4.3. Multi-Physical Field inside the Furnace

The arc is the most important energy source in a fused magnesia furnace, and its main heat transfer method is heat radiation, which plays an important role in the process of energy transfer and transformation. At the same time, it is difficult to measure the parameters of the arc directly. Therefore, it is of great significance to study the arc shape and determine the arc length, current density, joule heat, and temperature distribution.

4.3.1. Electromagnetic Field Distribution

In order to understand the distribution of the current density, the longitudinal section of the arc region is used to represent the range of the high-current region of the arc, and the cross-section of the arc region is used to represent the current flow and phase distribution between different electrodes. Figure 6a shows the ranges of the arc regions, which are spherically distributed and connected below the electrodes. According to the basic principle of three-phase electricity, the current flow of the three-phase current changes at any time, the current can flow in or out of each electrode, and the current always flows from high potential to low potential. The results of the time captured in this paper are shown in Figure 6b. The current flows from A into B and C, forming a closed loop with the arc plasma as a conductor. Due to the skin effect of the alternating current, the current density outside the section is significantly higher than that inside the section.

4.3.2. Arc Temperature Distribution

Figure 7a,b show the joule heat distribution of different sections in the fused magnesia furnace. Combined with the current density distribution in Figure 6, it is not difficult to see that the temperature distribution is closely related to the current density distribution, but there are some differences. The correlation shows that the current density directly affects the energy release power at the end of the electrode, and the input power can be directly adjusted by adjusting the current density. The difference is that the higher joule heat is at the position where the current flows out of the electrode, which indicates that the input power adjustment through the current density has a certain lag. At the same time, the high-temperature regions at the end of each electrode are connected to each other, which provides a stable energy source for a stable smelting process. These results provide a basis for the power regulation of a fused magnesia furnace.

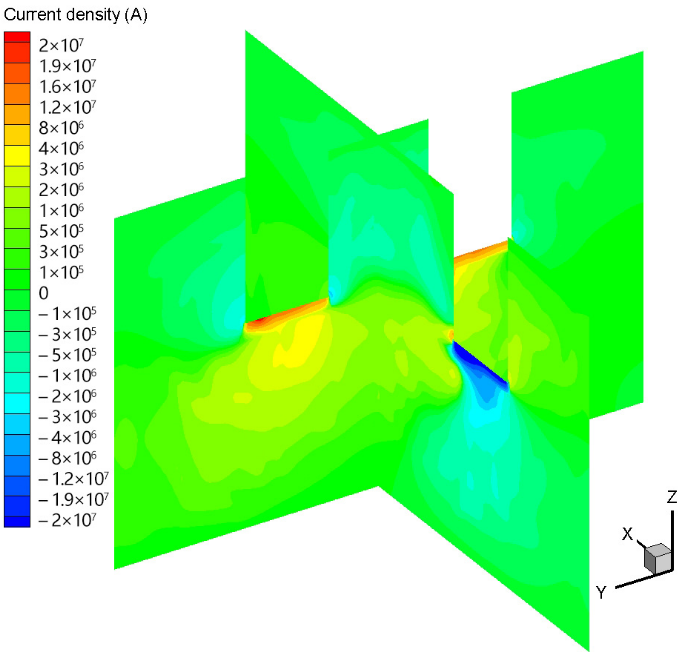

(a)

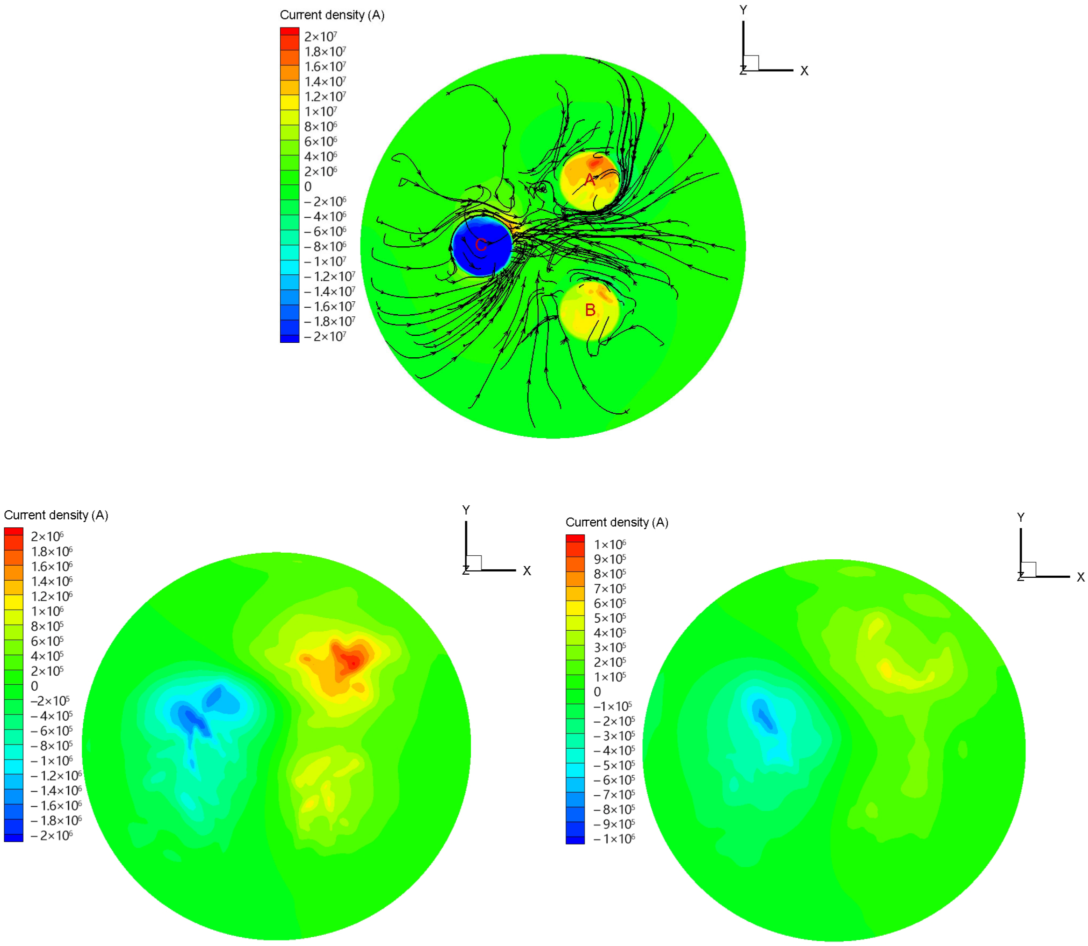

(b)

Figure 6. (**a**) Current density and flow direction (longitudinal section). (**b**) z = 0.65 m, 0.35 m, 0.15 m current densities and flow directions (cross-section).

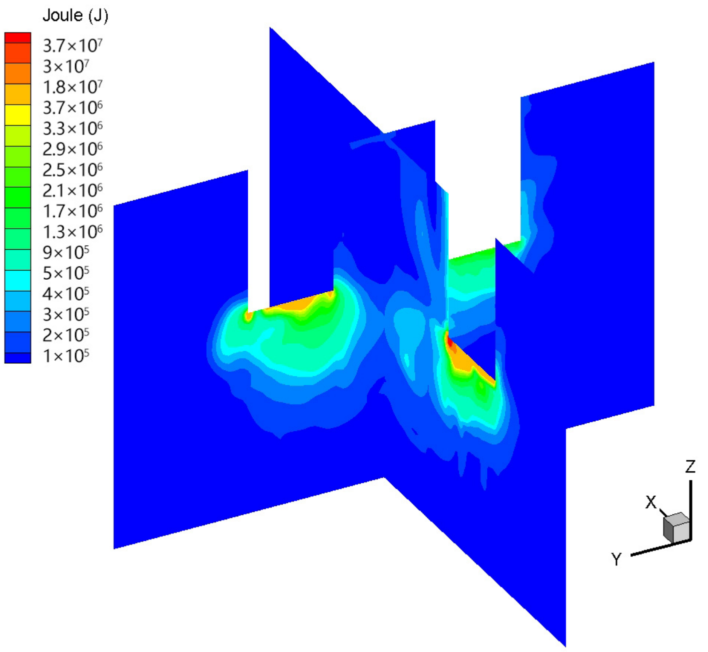

(**a**)

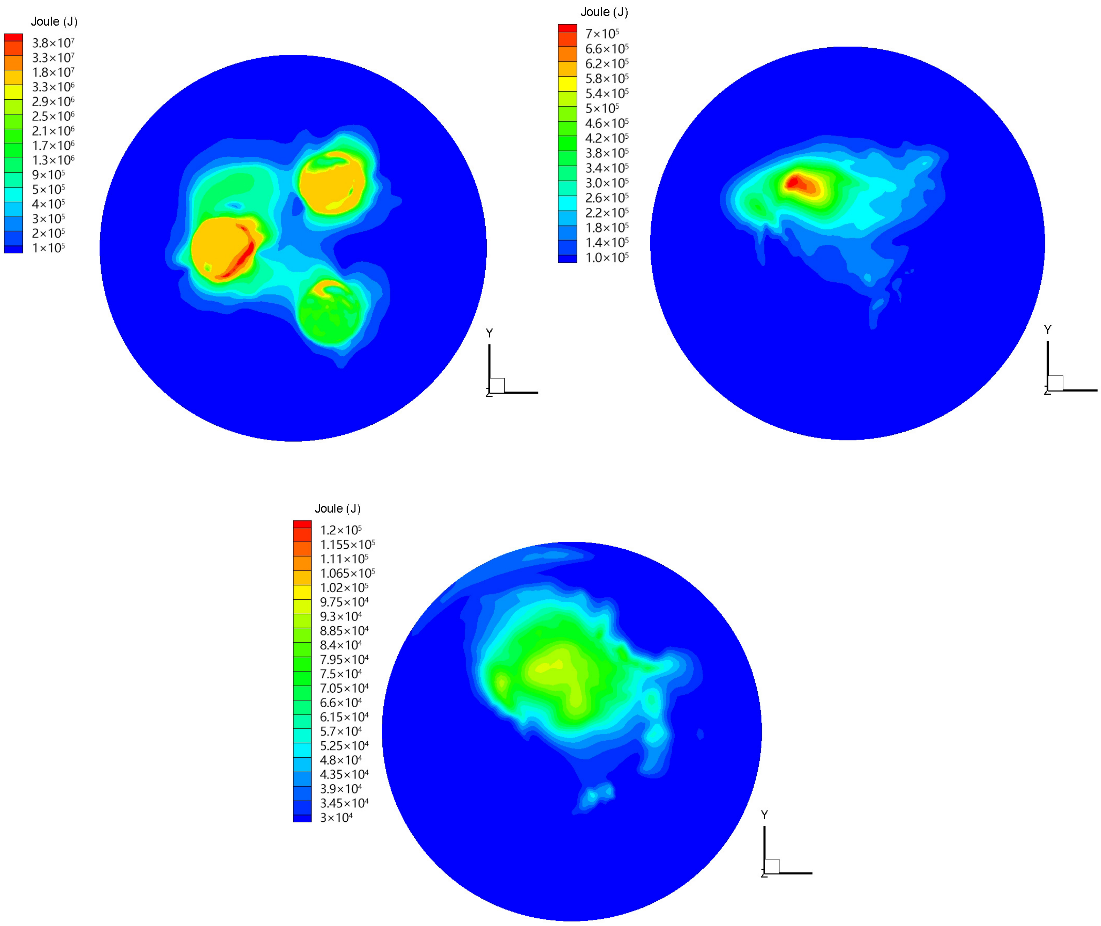

(**b**)

Figure 7. (**a**) Joule heat distribution (longitudinal section). (**b**) z = 0.65 m, 0.35 m, 0.15 m joule heat distributions (cross-section).

The temperature distribution in the arc area is shown in Figure 8a,b. The plasma part of the arc has the highest temperature and is in direct contact with the material, which provides the energy source for the decomposition and melting of magnesite. Influenced by the distribution of the current density and the rapid expansion of plasma, the high-temperature region forms a region with a high peripheral temperature and a low central temperature at the end of the three electrodes. The plasma regions of the three parts are connected to each other to form a closed loop, which provides a stable heat source for the smelting process. The maximum temperature in the inner arc zone is about 660 K, and the maximum temperature in the outer arc zone is 12,387 K. According to this phenomenon and production experience, it is reasonable to consider that the quality of the product outside the electrode may be higher than that in the center of the electrodes.

In addition, the arc length is one of the most important elements of the research. In this study, the special physical parameters of the fluid are considered in arc plasma. According to Reference 10, the excitation temperature of magnesium oxide gas is about 6700 K, so it is considered that the isothermal temperature of the electrode root distance of 6700 K is the arc length.

Figure 9a shows the temperature distribution at z = 0.65 m on the x-y section with different electrode insertion depths. It is obvious that, with an increase in the insertion depths from 0.4 m to 0.6 m, the maximum temperature increases from 8173 K to 13,120 K, the arc length increases from 0.048 m to 0.062 m, and the arc high-temperature diameter increases from 0.14 m to 0.16 m. In Figure 9b, the volume of the high-temperature area also increases slightly, but when the insertion depth is increased to 0.7 m, the maximum temperature decreases to 9723 K, and the range of the high-temperature area also decreases to 0.143 m, indicating that there must be an appropriate value for the electrode insertion depth to maximize the range of the arc area.

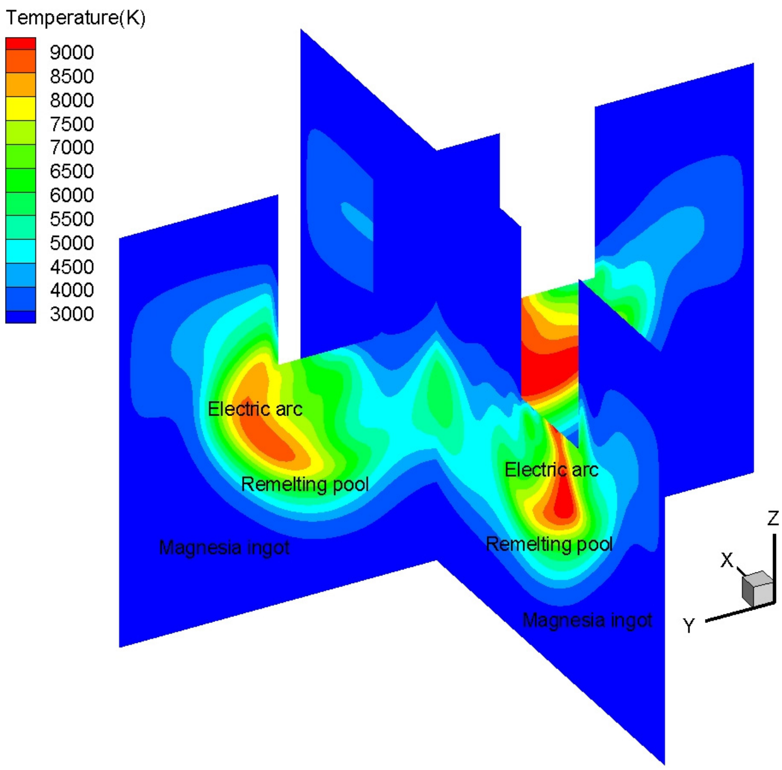

(**a**)

Figure 8. *Cont*.

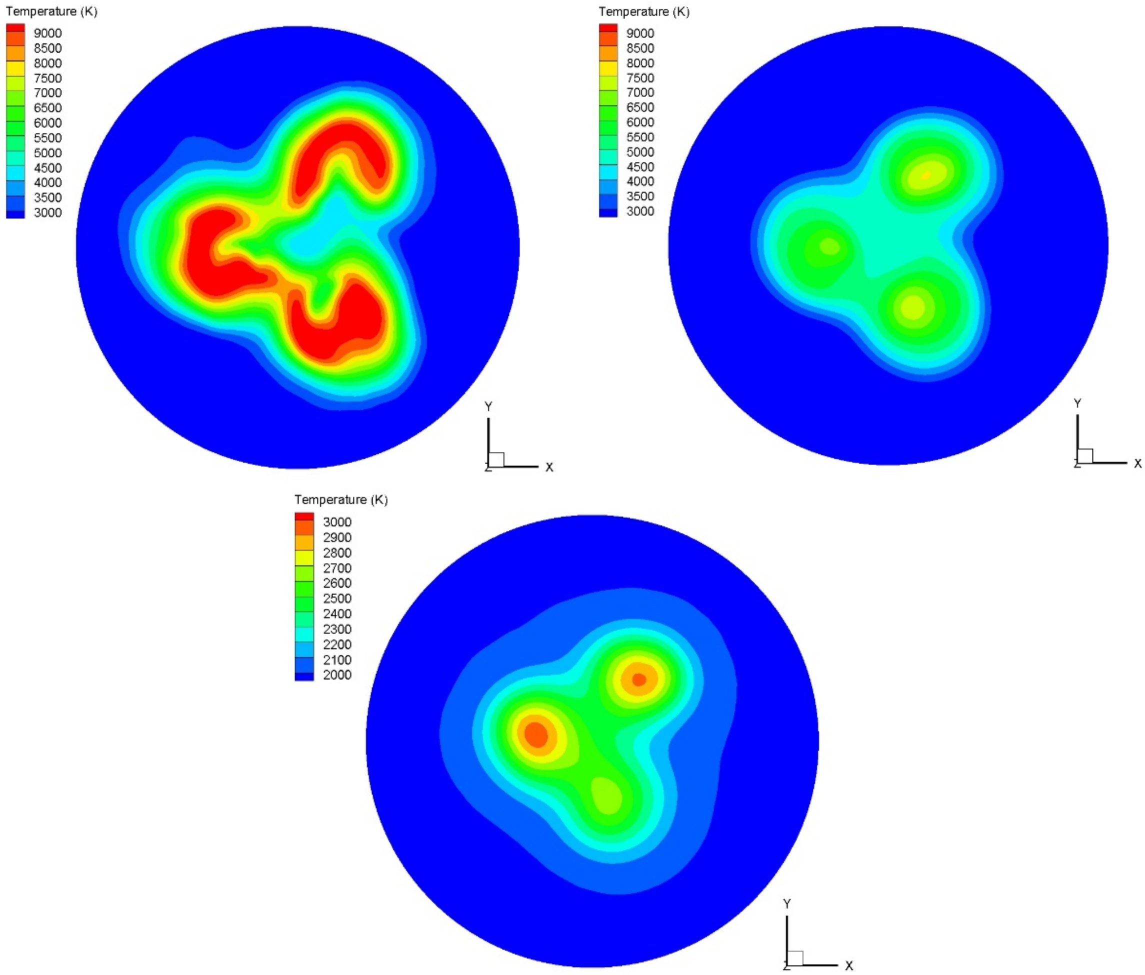

(**b**)

Figure 8. (**a**) Arc temperature distribution (longitudinal section). (**b**) z = 0.65 m, 0.35 m, 0.15 m arc temperature distributions (cross-section).

4.3.3. Reaction Distribution

A large amount of energy is used to decompose magnesite, and it is important to predict the decomposition properly. The main chemical reactions in the furnace are the decomposition of magnesium carbonate, and the decomposition of calcium carbonate and the reduction of iron oxide have little influence on the decomposition of magnesite.

Figure 10a,b show the decomposition of magnesite on the longitudinal section during the reaction. The main composition at the bottom of the furnace is magnesia, and the main composition at the top is the mixture of carbon dioxide and magnesite. The magnesite at the root of the electrode is largely decomposed into carbon dioxide, and this part of carbon dioxide diffuses upward to the accumulated ore area.

The calculation results of the different insertion depths are shown below. The results of Y = −0.65 m, Y = −0.15, and Y = 0 m are selected to represent the decomposition of the material area on the side, the decomposition of the arc area, and the decomposition of the low-temperature area in the center, respectively.

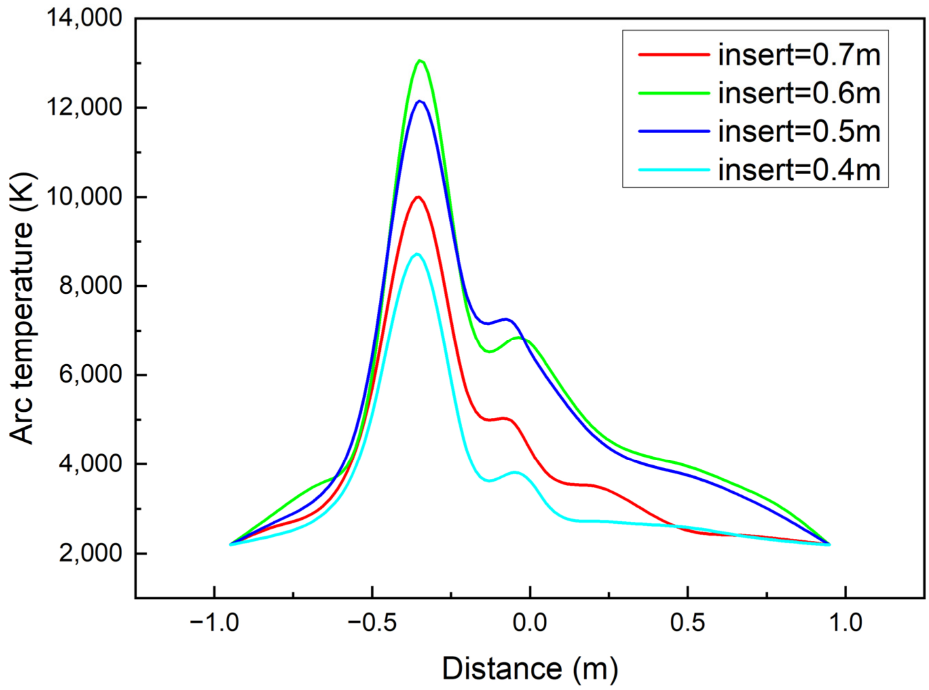

(**a**)

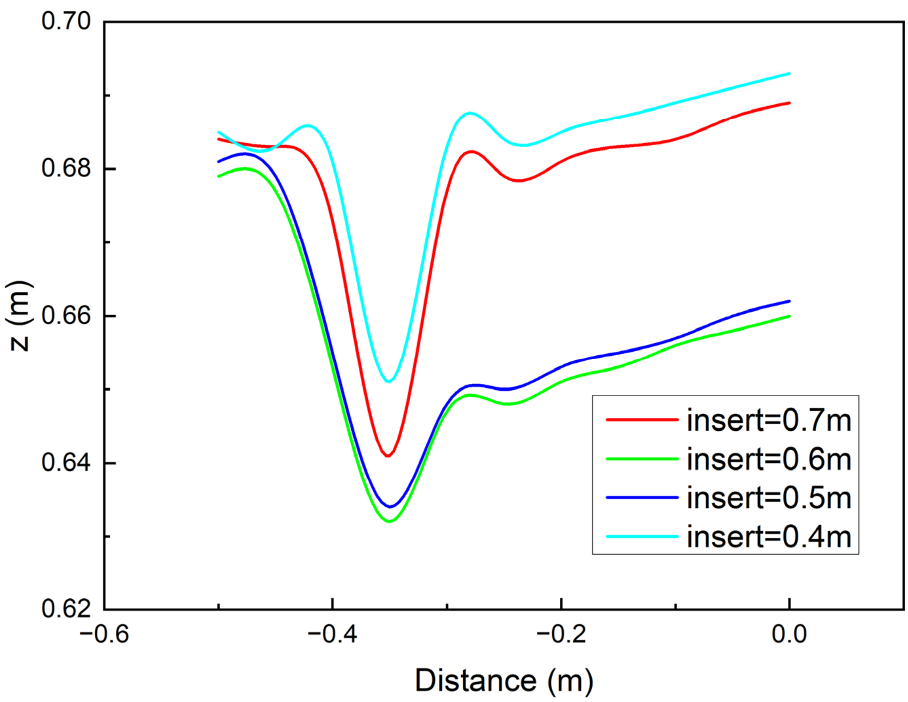

(**b**)

Figure 9. (**a**). Influence of insertion depth on temperature distribution of z = 0.65 m section. (**b**) Effect of penetration depth on arc length.

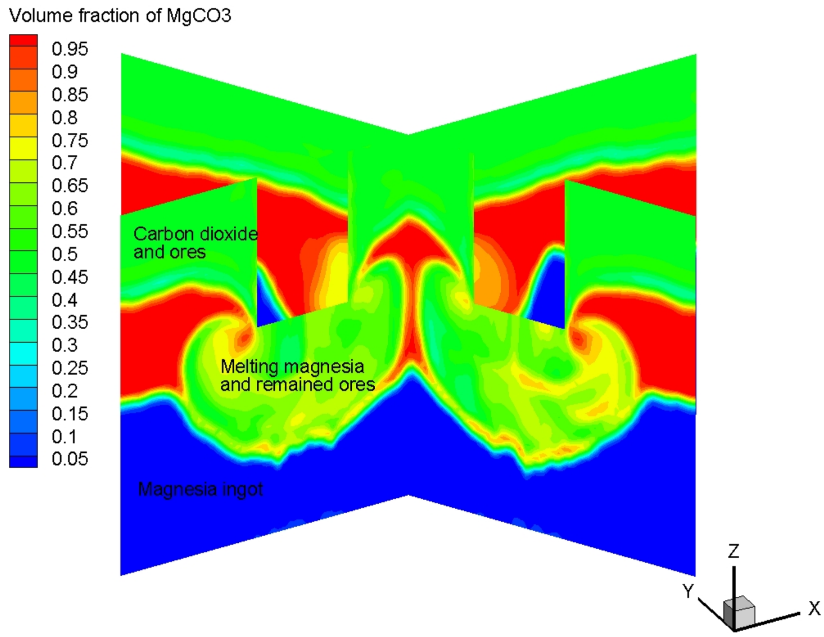

(**a**)

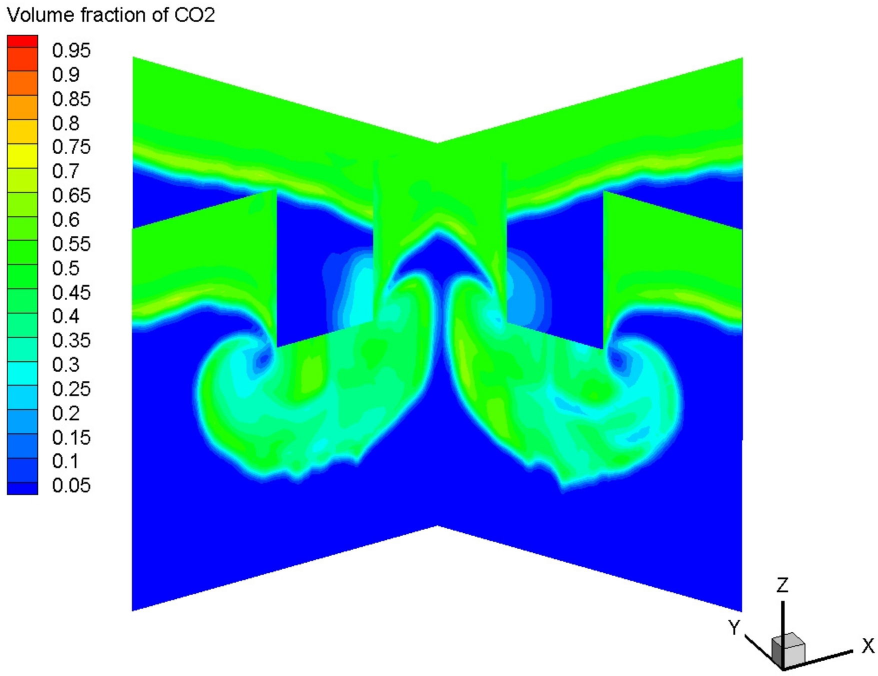

(**b**)

Figure 10. (**a**) Decomposition state of magnesium carbonate. (**b**) Carbon dioxide formation state.

Figure 11a shows the longitudinal component distribution at Y = −0.65 M on the x-z section. The main component at 0–0.3 m is magnesia (A), the main component at 0.4–0.7 m is undecomposed ore (B), and the accumulated ore at 0.8–1.2 m is carbon dioxide (C) filled in the gap after partial decomposition. As the insertion depth is increased from 0.4 m to 0.6 m, the height of A increases from 0.3 m to 0.4 m, and the composition of block B changes from only magnesite ore to a mixture of undecomposed ore and magnesium oxide. With an increase in the insertion depth, the decomposition degree increases. The content of carbon dioxide in block C increases with an increase in the insertion depth. However, when the insertion depth is increased to 0.7 m, the promoting effect on decomposition declines.

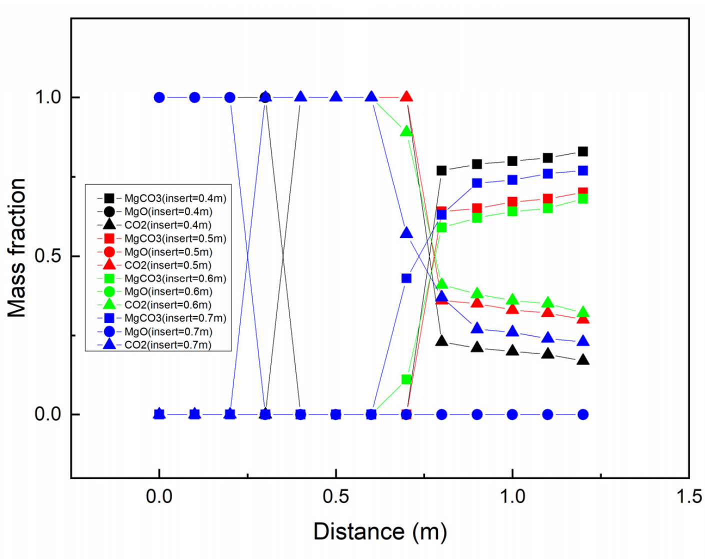

(**a**)

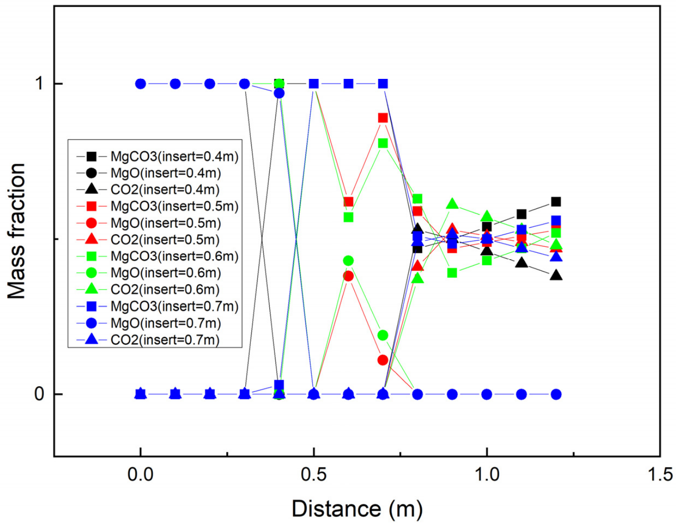

(**b**)

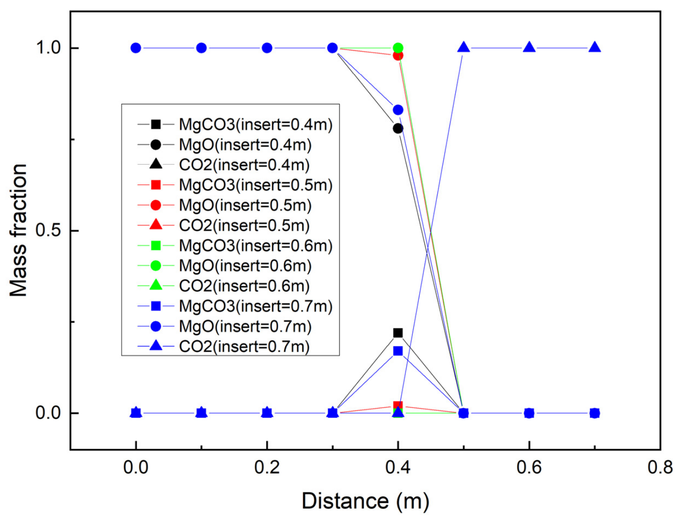

(**c**)

Figure 11. (**a**) Distribution of components at position Y = −0.65 m. (**b**) Distribution of components at position Y = −0.15 m. (**c**) Distribution of components at position Y = 0 m.

In Figure 11b, the longitudinal component distribution at Y = −0.15 m in the x–z section is shown, and the main component at 0–0.3 m is magnesia (A). The core area of decomposition is at 0.4–0.7 m, and the main component is carbon dioxide (B). When the electrode insertion depth is increased, the range of zone A basically remains unchanged, while the degree of decomposition in zone B increases. Similar to the previous results, the promoting effect of decomposition weakens when the insertion depth is 0.7 m.

In Figure 11c, the longitudinal component distribution at Y = 0 m in the x–z section is shown, and the main component at 0–0.3 m is magnesia (A). The connected arc area at 0.4–0.7 m is mainly composed of carbon dioxide (B). The 0.8 m to 1.2 m area contains the accumulated ore and the carbon dioxide (C) filled in the crevices after partial decomposition. With an increase in the insertion depth, the scope of area A shrinks, the position of area B decreases, and the scope of area C expands. An excessive penetration depth leads to a decrease in the decomposition degree of the ore deposited at the top, which has a negative impact on production.

5. Conclusions

In this paper, a three-dimensional transient multi-physical field model is established for the complex melting state of a magnesia furnace that included an electromagnetic field, turbulent flow, heat transfer, and a decomposition reaction. The arc is compared with that of the BOWMAN experiment, which verifies the reliability of the numerical model to some extent.

(1) In the process of melting magnesia, the current path is maintained through the connected arc area, and the current direction changes constantly. Because of the skin effect of the high-frequency alternating current, the current density distribution is not uniform. The current density along the medial side is significantly lower than along the lateral side.

(2) For ore decomposition, arc radiation heat is the main source. When the arc temperature is low, part of the ore and magnesium oxide mixture appears at the junction of the arc zone and magnesium oxide zone. At this time, low-temperature resistance heat is used to decompose the ore, which has a negative impact on the smelting process.

(3) The electrode insertion depth has an important influence on the decomposition and temperature distribution of magnesite. When the electrode insertion depth is increased from 0.4 m to 0.6 m, the maximum arc temperature increases to 13,065 K, the maximum arc length increases to 0.066 m, and the magnesite decomposition is more thorough. When the electrode insertion depth is too much, the arc temperature, the arc length, and the degree of magnesite decomposition decrease.

Author Contributions: Conceptualization, W.Z.; methodology, W.Z.; software, T.J.; validation, T.J.; formal analysis, T.J.; investigation, W.Z.; resources, T.J.; data curation, T.J.; writing—original draft preparation, T.J.; writing—review and editing, T.J.; visualization, W.Z.; supervision, W.Z.; project administration, W.Z.; funding acquisition, W.Z. All authors have read and agreed to the published version of the manuscript.

Funding: This research was funded by National Science Foundation of China grant number 2017YFA0700300.

Data Availability Statement: The experimental data in the paper were tested in Hai-Mei Magnesium Group, the data that support the findings of the study are available from the corresponding author upon reasonable request.

Conflicts of Interest: The authors declare no conflict of interest.

References

1. Chen, Q.; Wei, T. Development status and prospect of magnesium refractory materials in China. *Refract. Ries* **2013**, *47*, 210–214.
2. Jiang, X. Study on New Energy Saving Technology of Fused Magnesia and Crystallization Process of Magnesite in Magnesite Smelting. Master's Thesis, Northeastern University, Shenyang, China, 2011.
3. Jiang, T.; Zhang, W.; Liu, S. Performance Evaluation of a Full-Scale Fused Magnesia Furnace for MgO Production Based on Energy and Exergy Analysis. *Energies* **2021**, *15*, 214. [CrossRef]

4. Bowman, B.; Edels, H. Radial temperature measurements of alternating current arcs. *J. Phys. D Appl. Phys.* **1969**, *2*, 53. [CrossRef]
5. Wu, X.; Feng, Y.; Li, Y.; Li, Y.; Zhang, X.; Wu, C. Numerical simulation and orthogonal analysis on coupled arc with molten pool for keyholing plasma arc weld-ing. *Acta Metall. Sin.* **2015**, *51*, 1365–1376. [CrossRef]
6. Aula, M.; Demus, T.; Echterhof, T.; Huttula, M.; Pfeifer, H.; Fabritius, T. On-line Analysis of Cr2O3 Content of the Slag in Pilot Scale EAF by Measuring Optical Emission Spectrum of Electric Arc. *ISIJ Int.* **2017**, *57*, 478–486. [CrossRef]
7. Cayo, E.H.; Alfaro, S.C.A. Aplicabilidad del monitoreo de emisiones del arco eléctrico para el control de calidad en el proceso MAG-S. *Soldagem Inspeção* **2011**, *16*, 341–349. [CrossRef]
8. Almurr, J.; Bussière, W.; Hertzog, J.; Rochette, D. Numerical investigations on the electric arc behavior upon contact opening in a low-voltage switch under the effect of external magnetic field. *Electr. Power Syst. Res.* **2022**, *209*, 107945. [CrossRef]
9. Urusov, R.M.; Urusova, I. Numerical simulation of a helical shape electric arc in the external axial magnetic field. *Phys. Plasmas* **2016**, *23*, 103502. [CrossRef]
10. Chi, Z.; Zhang, W.; Yang, Q. Thermophysical properties of pure gases and mixtures at temperatures of 300–30,000 K and atmospheric pressure: Thermodynamic properties and solution of equilibrium compositions. *Plasma Sci. Technol.* **2021**, *23*, 125505. [CrossRef]
11. Deng, J.; Li, Y.; Xu, Y.; Sheng, H. Numerical Simulation of Fluid Flow and Heat Transfer in a DC Non-Transferred Arc Plasma Torch Operating Under Laminar and Turbulent Conditions. *Plasma Sci. Technol.* **2011**, *13*, 201. [CrossRef]
12. Wen, K.; Liu, X.; Zhou, K.; Liu, M.; Zhu, H.; Huang, J.; Zhang, Z.; Huang, R.; Mao, J.; Yan, X.; et al. 3D time-dependent numerical simulation for atmospheric plasma spraying. *Surf. Coatings Technol.* **2018**, *371*, 344–354. [CrossRef]
13. Wang, Z.; Wang, N.; Li, T.; Cao, Y. 3D Numerical Analysis of the Arc Plasma Behavior in a Submerged DC Electric Arc Furnace for the Production of Fused MgO. *Plasma Sci. Technol.* **2012**, *14*, 321–326. [CrossRef]
14. Wang, Z.; Fu, Y.; Wang, N.; Feng, L. 3D numerical simulation of electrical arc furnaces for the MgO production. *J. Mater. Process. Technol.* **2014**, *214*, 2284–2291. [CrossRef]
15. Yu, Y.; Li, B.; Yun, C.; Qi, F.; Liu, Z. Modeling on Reduction Reaction of Metal Oxides for Submerged Arc Furnace in Ferrochrome Pellets Smelting Process. *Met. Mater. Trans. A* **2021**, *52*, 3907–3919. [CrossRef]
16. Xi, X.; Chen, S.; Yang, S.; Ye, M.; Li, J. Melting Characteristics of Multipiece Steel Scrap in Liquid Steel. *ISIJ Int.* **2021**, *61*, 190–199. [CrossRef]
17. Logar, V.; Dovžan, D.; Škrjanc, I. Mathematical Modeling and Experimental Validation of an Electric Arc Furnace. *ISIJ Int.* **2011**, *51*, 382–391. [CrossRef]
18. Yang, Z.; Yang, L.; Cheng, T.; Chen, F.; Zheng, F.; Wang, S.; Guo, Y. Fluid Flow Characteristic of EAF Molten Steel with Different Bottom-Blowing Gas Flow Rate Distributions. *ISIJ Int.* **2020**, *60*, 1957–1967. [CrossRef]
19. Zhang, Z.; Chen, X.; Xu, J.; Shi, L. Numerical simulation on electromagnetic field, flow field and temperature field in semisolid slurry preparation by A-EMS. *Rare Met.* **2010**, *29*, 635–641. [CrossRef]
20. Wang, X.; Fan, D.; Huang, J.; Huang, Y. Numerical simulation of heat transfer and fluid flow in double electrodes TIG arc-weld pool. *Acta Met. Sin.* **2015**, *51*, 178–190.
21. Bakken, J.A.; Gu, L.; Larsen, H.L.; Sevastyanenko, V.G. Numerical modeling of electric arcs. *J. Eng. Phys.* **1997**, *70*, 530–543. [CrossRef]
22. Ranganathan, S.; Godiwalla, K.M. Influence of Process parameters on Reduction Contours during the production of Ferrochromium in Submerged-arc Furnace, Canadian Metallurgical Quarterly. *Can. Metall. Q.* **2011**, *50*, 37–44. [CrossRef]
23. Bowman, B. Measurements of plasma velocity distributions in free-burning DC arcs up to 2160 A. *J. Phys. D Appl. Phys.* **1972**, *5*, 1422. [CrossRef]